



This is a repository copy of *3D magnetohydrodynamic wave propagation and energy transport in a simulated solar vortex*.

White Rose Research Online URL for this paper:

<https://eprints.whiterose.ac.uk/229157/>

Version: Published Version

Article:

Skirvin, S.J. orcid.org/0000-0002-3814-4232, Fedun, V. orcid.org/0000-0002-0893-7346, Verth, G. orcid.org/0000-0002-9546-2368 et al. (1 more author) (2025) 3D magnetohydrodynamic wave propagation and energy transport in a simulated solar vortex. The Astrophysical Journal, 988 (1). 18. ISSN 0004-637X

<https://doi.org/10.3847/1538-4357/adce73>

Reuse

This article is distributed under the terms of the Creative Commons Attribution (CC BY) licence. This licence allows you to distribute, remix, tweak, and build upon the work, even commercially, as long as you credit the authors for the original work. More information and the full terms of the licence here:

<https://creativecommons.org/licenses/>

Takedown

If you consider content in White Rose Research Online to be in breach of UK law, please notify us by emailing eprints@whiterose.ac.uk including the URL of the record and the reason for the withdrawal request.



eprints@whiterose.ac.uk
<https://eprints.whiterose.ac.uk/>



3D Magnetohydrodynamic Wave Propagation and Energy Transport in a Simulated Solar Vortex

Samuel J. Skirvin¹ , Viktor Fedun¹ , Gary Verth² , and Istvan Ballai² ¹ Plasma Dynamics Group, School of Electrical and Electronic Engineering, University of Sheffield, Sheffield, S1 3JD, UK; samuel.j.skirvin@northumbria.ac.uk, v.fedun@sheffield.ac.uk² Plasma Dynamics Group, School of Mathematical and Physical Sciences, University of Sheffield, Sheffield S3 7RH, UK; g.verth@sheffield.ac.uk, i.ballai@sheffield.ac.uk

Received 2025 February 20; revised 2025 April 14; accepted 2025 April 16; published 2025 July 10

Abstract

Magnetic flux tubes in the presence of background rotational flows are abundant throughout the solar atmosphere and may act as conduits for MHD waves to transport energy throughout the solar atmosphere. Here we investigate the contribution from MHD waves to the Poynting flux in a 3D numerical simulation of a realistic solar atmosphere, modeling a structure resembling a solar vortex tube, using the PLUTO code in the presence of different plasma flow configurations. These simulations feature a closed magnetic loop system where a rotational flow is imposed at one footpoint in addition to photospheric perturbations acting as a wave driver mimicking those of p -modes. We find that a variety of MHD waves exist within the vortex tube, including sausage, kink, and torsional Alfvén waves, owing to the photospheric wave driver and the nature of the rotational flow itself. We demonstrate how the visual interpretation of different MHD modes becomes nontrivial when a background rotational flow is present compared to a static flux tube. By conducting a simulation both with and without the rotational plasma flow, we demonstrate how the perturbed Poynting flux increases in the presence of the rotational flow as the waves transport increased magnetic energy. We attribute this increase to the dynamical pressure from the rotational flow increasing the plasma density at the tube boundary, which acts to trap the wave energy more effectively inside the vortex. Moreover, we demonstrate how the Poynting flux is always directed upward in weakly twisted magnetic flux tubes.

Unified Astronomy Thesaurus concepts: [Magnetohydrodynamics \(1964\)](#); [Solar atmosphere \(1477\)](#); [Solar chromosphere \(1479\)](#); [Solar oscillations \(1515\)](#)

1. Introduction

The solar magnetic field, coupled with dynamical plasma motions at the photosphere, is known to play a major role in the transport of energy to the solar corona, which is ultimately responsible for heating coronal plasma to millions of degrees (J. A. Klimchuk 2006). One of the possible ways that energy can be transported is through the propagation of magnetohydrodynamic (MHD) waves in various magnetic structures, supported by gradients in the magnetic field or other plasma diagnostics (T. Van Doorsselaere et al. 2020).

Solar vortices are ubiquitous throughout the solar atmosphere (D. B. Jess et al. 2015; S. Skirvin et al. 2023; K. Tziotziou et al. 2023), and small-scale swirling motions occur naturally in the photosphere within the intergranular lanes (J. A. Bonet et al. 2008; S. Shelyag et al. 2011; I. Giagkiozis et al. 2018) in addition to magnetic structures that display rotational behavior (e.g., W. Curdt & H. Tian 2011; Y. Su et al. 2014; R. Sharma et al. 2018; S. Skirvin et al. 2023). Photospheric swirling motions have been suggested as a source of incompressible torsional Alfvén waves in the solar atmosphere (V. Fedun et al. 2011b; R. J. Morton et al. 2013; N. Yadav et al. 2021; D. B. Jess et al. 2023). Moreover, solar vortex tubes have been reported to harbor oscillations that may be interpreted as MHD waves (K. Tziotziou et al. 2018, 2020; M. Murabito et al. 2020). While it is becoming more evident that rotating structures can support MHD waves in the solar

atmosphere, there are few studies investigating the potential for solar vortex tubes to transport MHD wave energy or how MHD waves may manifest themselves in such structures (S. J. Skirvin et al. 2023a).

Recent analytical work (S. J. Skirvin et al. 2024a) has demonstrated that MHD waves carry an increased amount of field-aligned Poynting flux in the presence of background rotational flows and that the flux increase is dependent upon the amplitude ratio between the strengths of the flow and the perturbation. Additionally, numerical simulations have shown that the Poynting flux is enhanced in regions where solar vortices are present, in the form of either solar tornadoes or small-scale vortices within the solar plage (N. Yadav et al. 2020, 2021; A. J. Finley et al. 2022; H. Kuniyoshi et al. 2023). Numerical simulations of a magnetic tornado structure in the solar atmosphere (S. Wedemeyer-Böhm et al. 2012) concluded that vortices contain 14 kW m^{-2} of vertical Poynting flux with a net upward flux of 400 W m^{-2} . However, in these studies, the authors did not elaborate on the possibility for the enhanced Poynting flux to be transported from supported MHD wave propagation within the vortex structure or attempt to separate the vertical Poynting flux associated with the vortex structure itself from the Poynting flux carried by MHD waves. In both numerical magnetoconvection simulations and solar observations, it is difficult to separate the background plasma motions from any perturbations (e.g., waves) from the full field vectors. Our work presents a first attempt at conducting full 3D modeling of MHD waves in a magnetic flux tube in the presence of a background vortical flow, with the aim to dissect the properties and energy associated with MHD wave propagation.



Original content from this work may be used under the terms of the [Creative Commons Attribution 4.0 licence](#). Any further distribution of this work must maintain attribution to the author(s) and the title of the work, journal citation and DOI.

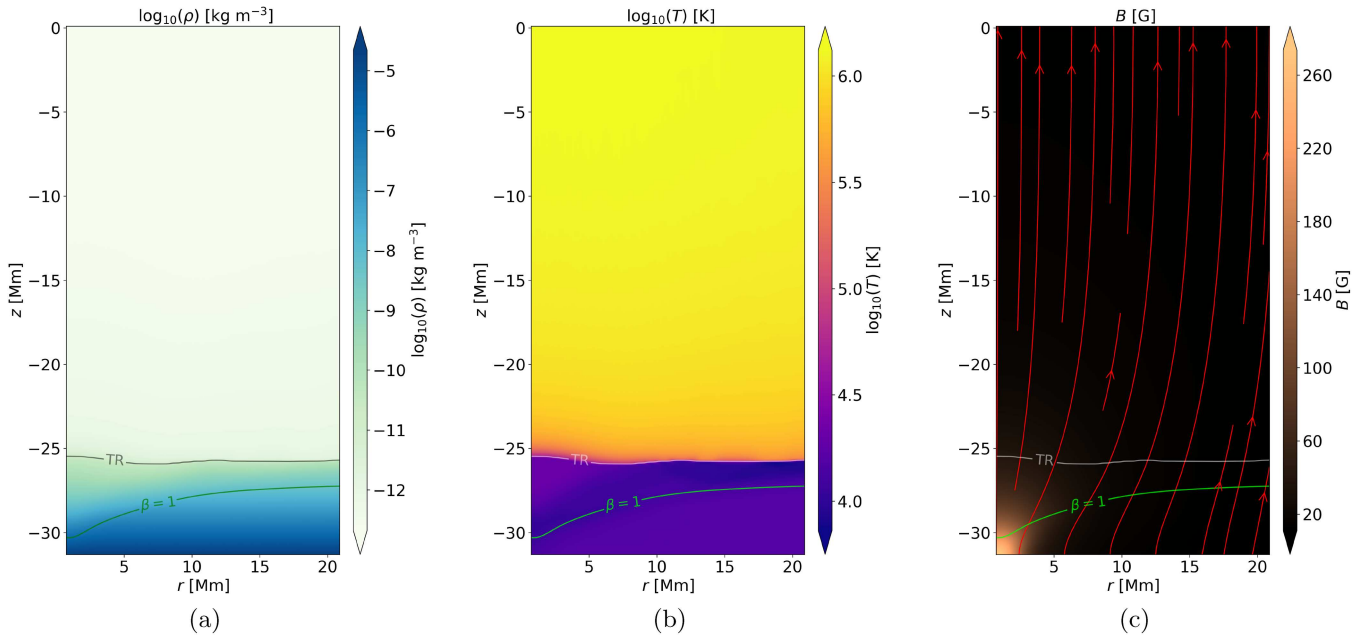


Figure 1. The equilibrium configuration displaying the (a) plasma density, (b) plasma temperature, and (c) magnetic field strength and structure in the 3D loop model. This corresponds to a snapshot at the initial stage of the simulation before any flow or wave driver is introduced and is taken at an azimuthal slice of $\varphi = \pi/2$. The TR and plasma- $\beta = 1$ contours are also highlighted in each plot. This figure shows a subsection of the full numerical domain for illustration purposes.

Our paper is structured as follows. In Section 2, we describe the numerical model used in the current study and the creation of a 3D solar vortex tube, in addition to introducing the modeled wave driver. Section 3 describes the results of the current study investigating the MHD waves present in the vortex tube and their different generation mechanisms. Furthermore, we present results on the Poynting flux in the vortex tube and the contribution to this flux from MHD waves. Section 4 summarizes the results and outlines avenues for future work.

2. Methods

2.1. Model

The 3D numerical model adopted in this work was introduced by F. Reale et al. (2016) featuring a straightened, evacuated loop spanning from photosphere to photosphere in a cylindrical coordinate system (r, φ, z) . The simulation domain ranges from 0.73 Mm to 41.01 Mm in the radial direction, from 0 to π in the φ -direction, and from -31.31 Mm to 31.31 Mm in the z -direction, with $192 \times 256 \times 768$ data points, respectively. The original thermodynamic model is adapted from S. Serio et al. (1981) for closed coronal loop models, and the initial equilibrium is obtained by numerically relaxing a hydrostatic model over time, with vertical and straight magnetic fields, as outlined in M. Guarrasi et al. (2014). As a result of increased plasma and magnetic pressure at the center of the loop, the magnetic field ultimately expands in the corona during the equilibration process. At the footpoints, the magnetic field has a maximum strength of 273 G, which decreases to 13 G at the loop apex at $z = 0$ Mm (see Figure 1(c)), which is appropriate for quiet Sun conditions of the network field. Furthermore, the total magnetic field decreases with radial distance across the loop, and its magnitude has a profile that is approximately Gaussian-shaped. For more information regarding the numerical domain

and setup, we refer readers to earlier studies by J. M. Riedl et al. (2021) and S. J. Skirvin et al. (2023b, 2024b).

Gravity is incorporated into the model in the form

$$g(z) = -g_{\odot} \cos\left(\frac{(z - z_0)\pi}{L}\right), \quad (1)$$

where $g_{\odot} = 274 \text{ m s}^{-2}$ is the gravitational acceleration at the solar surface, z_0 is the z -coordinate of the photosphere located at the base of our numerical domain, and $L = 61.61$ Mm is the total length of the loop. Taking a gravitational profile in this form results in a gravitational acceleration acting in the negative z -direction for $z < 0$ and the positive z -direction for $z > 0$ with $g(0) = 0 \text{ m s}^{-2}$ at the loop apex. Both the gravity across the loop and the loop curvature are neglected.

The initial model is presented in Figure 1, highlighting the plasma density and temperature, in addition to the plasma- $\beta = 1$ contour along with the position of the transition region (TR), which, for simplicity, is defined as the location where the plasma temperature $T = 40,000$ K. However as the TR has a finite width, the TR contour should be regarded as an approximation. The width of the TR is roughly 1 Mm, which is broader than theoretically expected but much narrower than some numerical models (e.g., G. Pelouze et al. 2023; K. Karampelas & T. Van Doorselaere 2024). Therefore, the TR will still act as a wave barrier but may allow for more transmission of energy flux than expected. We also display the strength and structure of the magnetic field in Figure 1(c), which exhibits an expanding flux tube structure below the TR where the density stratification is strong. The magnetic field is directed from the footpoint at the bottom boundary to the opposite footpoint at the upper boundary.

2.2. Numerical Setup and Boundary Conditions

As we are interested in studying MHD waves in the presence of rotational flows, a full 3D cylinder (2π in the azimuthal direction) is modeled in the current work. This

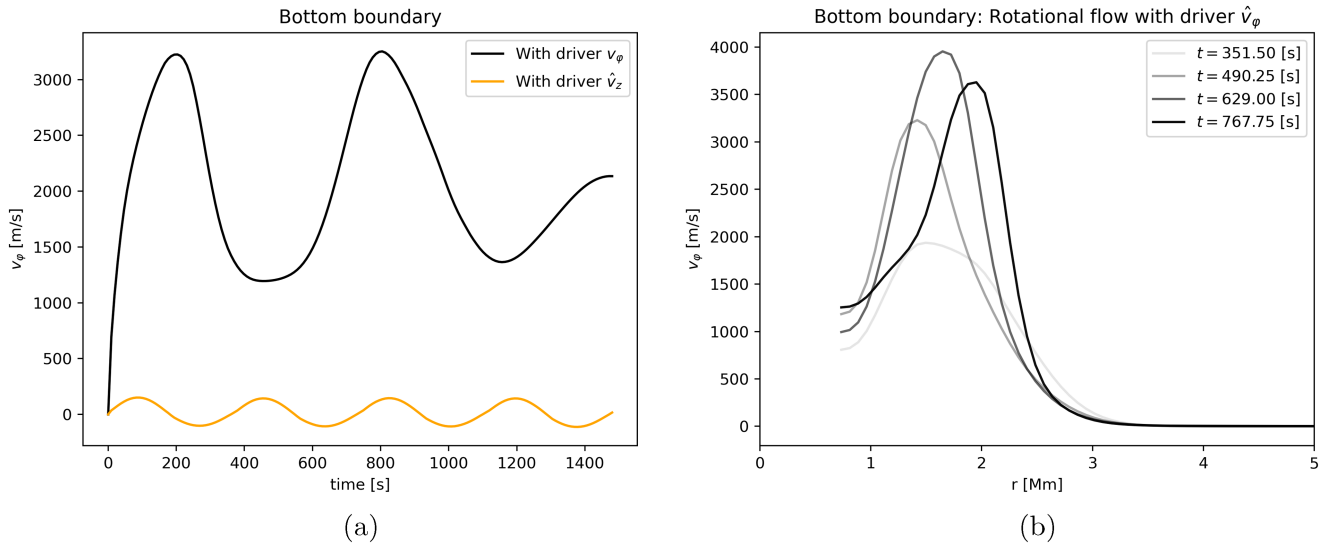


Figure 2. Plots at the bottom boundary of the domain showing (a) the temporal evolution of the total azimuthal velocity (v_ϕ) and perturbation of the vertical component of the velocity (\hat{v}_z) from the wave driver at $r = 2.10$ Mm. Panel (b) highlights the spatial profile of the rotational flow applied at the bottom boundary at different time snapshots, depicted in the legend.

differs from previous simulations utilizing the same model, where only one-fourth (F. Reale et al. 2016; J. M. Riedl et al. 2021) or half of the loop (S. J. Skirvin et al. 2023b, 2024b) was considered. Our simulation domain ranges from 0.73 Mm to 41.01 Mm in the radial direction, from 0 to 2π in the φ -direction, and from -31.31 Mm to 31.31 Mm in the z -direction, with $192 \times 512 \times 768$ data points, respectively. The loop axis is located at $r = 0$ Mm; however, we do not simulate the domain close to this region due to the singularity at the origin of the domain. The loop apex is located at $z = 0$ Mm. The numerical mesh is stretched in the radial and vertical directions in certain regimes of the domain to ensure that increased resolution is obtained closer to the enhanced region of the magnetic field, whereas decreased resolution is utilized in regions of low stratification such as the upper corona and at large radial distances away from the center of the magnetic loop. The mesh and resulting resolution are uniform in the azimuthal direction. An exact description of the numerical grid and resolution in different regimes can be found in J. M. Riedl et al. (2021).

The simulations are performed using the PLUTO code (A. Mignone et al. 2007, 2012, 2018), where the ideal MHD equations are solved in 3D cylindrical coordinates using the Harten–Lax–Van Leer approximate Riemann solver, with a piecewise total variation diminishing linear reconstruction method for the spatial integration. Field-aligned thermal conduction is included in the model; however, nonideal effects such as viscosity, resistivity, and radiative cooling are ignored. We utilize reflective boundary conditions for both boundaries in the r -direction and symmetric boundary conditions in the φ -direction. Additionally, we incorporate antisymmetric boundaries for the upper boundary. At the lower boundary, the same boundary conditions are set; however, the velocity, pressure, and density are perturbed according to an analytical solution for a gravity-acoustic wave, given in Section 2.4.

2.3. Forming a 3D Solar Vortex Tube

To create a structure resembling a solar vortex tube, we introduce a velocity perturbation at the bottom boundary in the

azimuthal component, v_ϕ , representing one footpoint of the loop. From this point forward, we will refer to the magnetic structure as a vortex tube, which is created by modeling a rotational flow inside the magnetic loop. This perturbation introduces a twisting of the velocity at the photospheric level. Due to the high plasma- β here ($\beta \gg 1$), the magnetic field is tied to the plasma motions; as such, B_ϕ are naturally generated at the lower boundary but are less pronounced at greater heights. These rotational perturbations are commonplace in the solar photosphere and naturally appear in the intergranular lanes (I. Giagkiozis et al. 2018). The torsional flow, in the horizontal plane at the bottom boundary, takes the form (N. Magyar et al. 2021)

$$v_\phi(r, t) = f(t) \cdot A e^{-(r-r_s)/r_b)^2}, \quad (2)$$

where A represents the flow amplitude, taken to be 1 km s^{-1} ; r_s denotes the center of the Gaussian; and r_b is the width of the flow in the horizontal plane. The width of the Gaussian in Equation (2) results in an azimuthal flow in a narrow ring of r_b around r_s . We set $r_b = 750 \text{ km}$ and $r_s = 1.75 \text{ Mm}$, which results in a vortex flow driven off-center from the magnetic field enhancement at one footpoint. The time behavior of the torsional flow is given by the function $f(t)$ and models a decaying vortex. The analytical form of this function is given by $f(t) = \exp^{-(t/\tau)^8}$, where $\tau = 270 \text{ s}$ represents the characteristic driving time (N. Magyar et al. 2021).

The temporal evolution of the velocity perturbation at the bottom boundary is displayed in Figure 2(a). The profile of v_ϕ demonstrates a unique periodicity that is not defined in Equation (2) and is a result of the boundary condition at the inner radial boundary. As the simulation domain does not cover the axis of the tube, the inner radial boundary is located at $r = 0.71 \text{ Mm}$ with a reflective boundary condition. As a result, the azimuthal motions are tied to this location and experience a reflection as the vortex begins to decay. While this physical effect is not intended in the simulation, it can mimic the temporal behavior of a realistic solar vortex within intergranular lanes in the photosphere that constantly experiences buffeting motions from nearby granules affecting its

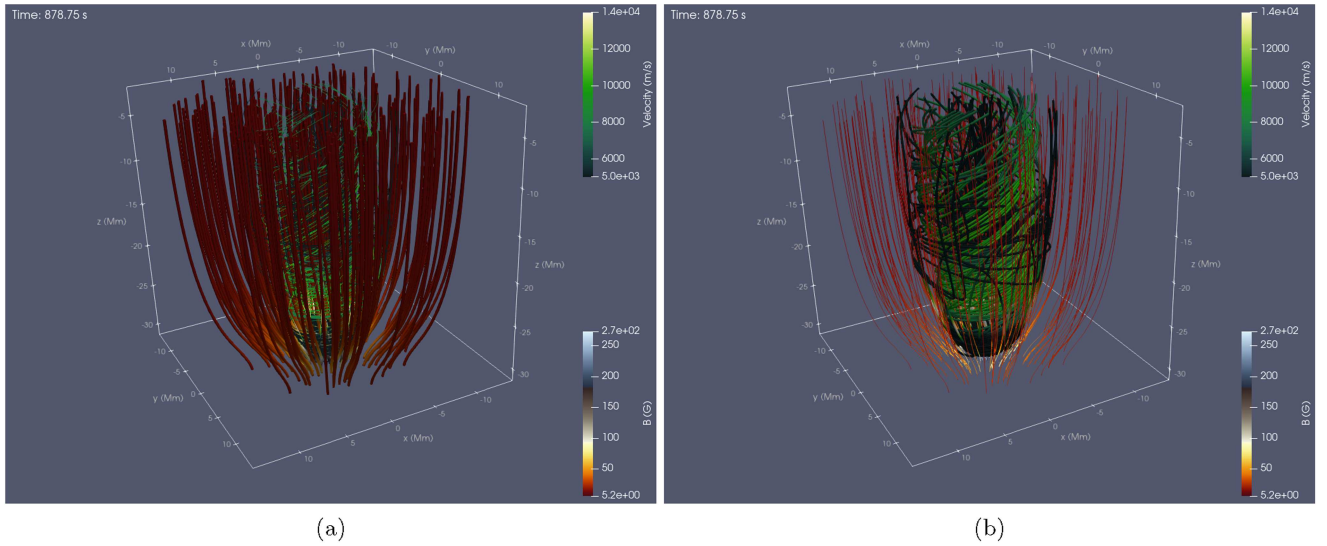


Figure 3. Snapshot of the 3D streamlines at $t = 879$ s of the magnetic field (predominantly red color) and velocity field (predominantly green color) for the generated vortex tube in a box outlining the numerical domain from the bottom boundary to the apex. Panel (a) shows the magnetic field as a 3D tube, whereas panel (b) highlights the velocity field as a 3D tube.

rotational speed. This effect is only present in the radial dependence of the flow as Equation (2) is independent of φ and the azimuthal boundary conditions are symmetric. Ultimately, this effect acts as an additional incompressible wave driver and is discussed in more detail in Section 3.3. In fact, it is likely that the buffeting experienced by vortices in the intergranular lanes is also nonaxisymmetric in nature (unlike the axisymmetric rotational flow considered in this work), which will act to excite higher-order modes of different polarization. Figure 2(a) also displays the amplitude of \hat{v}_z associated with the photospheric wave driver as a function of time. The clear periodicity of the wave driver is observed, which is discussed in more detail in Section 2.4.

Furthermore, the spatial distribution of the rotational flow applied at the bottom boundary is displayed in Figure 2(b) for four time snapshots. The location of the inner boundary at $r = 0.71$ Mm is evident in this plot, and it is clear that the Gaussian shape of the v_φ component behaves as expected. The maximum amplitude the flow obtains is around 4 km s^{-1} . It is worth noting that the rotational flow introduced is torsional in nature, i.e., $\partial/\partial\varphi = 0$, and that the flow is strictly polarized in the azimuthal direction.

Snapshots of the full 3D magnetic and velocity streamlines are displayed in Figures 3(a) and 3(b), respectively. This figure highlights the structure of both magnetic and velocity fields resulting from the v_φ flow applied at the bottom boundary. As the magnetic Reynolds number does not get large enough in the simulation domain for the magnetic field to be advected with the flow, the field lines remain relatively straight and untwisted; however, a very small twist can be observed at the bottom boundary, where the flow is introduced. With height, the plasma enters the $\beta \ll 1$ regime, and the magnetic field ultimately dominates the dynamics of the plasma, resulting in a relatively straight magnetic field in a rotational background plasma flow following a helical structure resulting from a combination of the vertical magnetic field and the v_φ component of the flow. The strength of the flow is too weak in the corona to influence the magnetic field and creates a rotating structure in a straight magnetic field, properties that are reminiscent of solar vortex tubes appearing naturally in

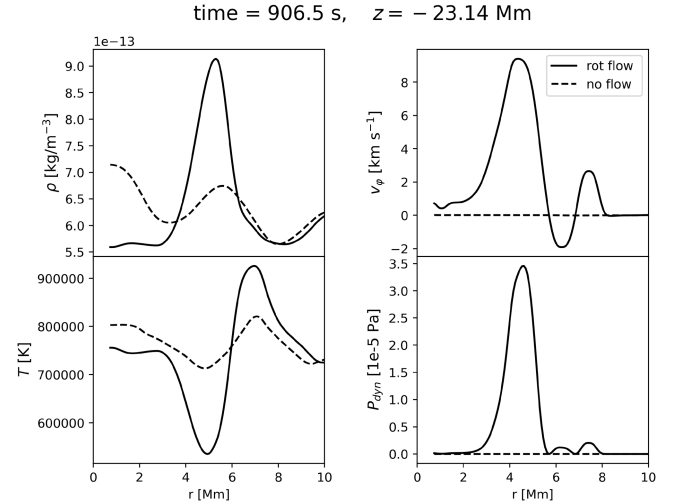


Figure 4. Transverse profiles of the plasma density (top left), rotational component of the velocity (top right), plasma temperature (bottom left), and dynamical pressure (bottom right) in the corona at $t = 906.5$ s for simulations with (solid line) and without (dashed line) a rotational flow. These plots are for the simulations excluding a photospheric wave driver, i.e., only consider the effect of the rotational flow.

magnetoconvection simulations (S. Wedemeyer & O. Steiner 2014; S. S. A. Silva et al. 2020). This is particularly important to emphasize because it is traditional to assume that the coronal magnetic field is twisted when traced back to the photospheric footpoints where a vortical flow is present in observations. However, it is clear in this simulation that, even when a rotational flow is applied in the photosphere, the magnetic field remains largely untwisted in the corona, whereas it is the plasma velocity that displays a stronger signature of a twisted nature.

Figure 4 displays the transverse structuring of the plasma density, temperature, rotational flow, and dynamical pressure for the simulations with and without the rotational flow (excluding the wave driver). The presence of a rotational flow creates a layer of denser and cooler plasma localized within a thin region (1–2 Mm) where the rotational flow reaches a

maximum at the edge of the vortex. This can be understood by considering the effect of dynamical pressure P_{dyn} . The dynamical pressure arises from the conservation of fluid momentum in a moving fluid and is defined as $P_{\text{dyn}} = v_\varphi^2 \rho / 2$. The dynamical pressure compresses the plasma where the rotational flow is strong, resulting in a layer of cool dense plasma that may be considered as an enhanced waveguide and will be discussed later in terms of supporting wave propagation. Throughout this study, we will compare the simulations when the rotational flow is included as opposed to when there is no rotational flow present; however, it should be noted that the presence of a rotational flow alters the plasma conditions, so care should be taken to make a complete direct comparison.

2.4. Wave Driver

In addition to the rotational flow outlined in Section 2.3, we also incorporate a gravity-acoustic wave driver that perturbs all components of the velocity vector as well as the plasma pressure and density, taking the form (D. Mihalas & B. W. Mihalas 1984; E. Khomenko & P. S. Cally 2012; I. C. Santamaria et al. 2015; J. M. Riedl et al. 2021; S. J. Skirvin et al. 2023b)

$$\hat{v}_r = A|v| \exp\left(\frac{z}{2H} + \Im(k_z)z\right) \cos(\varphi) \times \sin(\omega t - \Re(k_z)z - k_\perp r \cos(\varphi) + \phi_v), \quad (3)$$

$$\hat{v}_\varphi = -A|v| \exp\left(\frac{z}{2H} + \Im(k_z)z\right) \sin(\varphi) \times \sin(\omega t - \Re(k_z)z - k_\perp r \cos(\varphi) + \phi_v), \quad (4)$$

$$\hat{v}_z = A \exp\left(\frac{z}{2H} + \Im(k_z)z\right) \times \sin(\omega t - \Re(k_z)z - k_\perp r \cos(\varphi)), \quad (5)$$

$$\hat{p} = A|P| \exp\left(\frac{z}{2H} + \Im(k_z)z\right) \times \sin(\omega t - \Re(k_z)z - k_\perp r \cos(\varphi) + \phi_p), \quad (6)$$

$$\hat{\rho} = A|\rho| \exp\left(\frac{z}{2H} + \Im(k_z)z\right) \times \sin(\omega t - \Re(k_z)z - k_\perp r \cos(\varphi) + \phi_\rho), \quad (7)$$

where

$$|v| = \frac{c_s^2 k_\perp}{(\omega^2 - c_s^2 k_\perp^2)} \sqrt{\Re(k_z)^2 + \left(\Im(k_z) + \frac{\gamma - 2}{2H\gamma}\right)^2}, \quad (8)$$

$$|P| = \frac{\gamma\omega}{(\omega^2 - c_s^2 k_\perp^2)} \sqrt{\Re(k_z)^2 + \left(\Im(k_z) + \frac{\gamma - 2}{2H\gamma}\right)^2}, \quad (9)$$

$$|\rho| = \frac{\omega}{(\omega^2 - c_s^2 k_\perp^2)} \times \sqrt{\Re(k_z)^2 + \left(\Im(k_z) - \frac{1}{2H} + \frac{\gamma - 1}{H\gamma} \frac{k_\perp^2 c_s^2}{\omega^2}\right)^2}, \quad (10)$$

$$k_r = \cos(\varphi) \sin(\theta) \left| \frac{\omega}{c_s} \sqrt{\frac{(\omega_c^2 - \omega^2)}{(\omega_g^2 \sin(\theta)^2 - \omega^2)}} \right|, \quad (11)$$

$$k_\varphi = \sin(\varphi) \sin(\theta) \left| \frac{\omega}{c_s} \sqrt{\frac{(\omega_c^2 - \omega^2)}{(\omega_g^2 \sin(\theta)^2 - \omega^2)}} \right|, \quad (12)$$

$$k_\perp = \sqrt{k_r^2 + k_\varphi^2}, \quad (13)$$

$$k_z = \sqrt{\frac{\omega^2 - \omega_c^2}{c_s^2} - k_\perp^2 \frac{\omega^2 - \omega_g^2}{\omega^2}}, \quad (14)$$

$$\omega_c = \frac{c_s}{2H} \cos(\theta_B), \quad (15)$$

$$\omega_g = \frac{2\omega_c \sqrt{\gamma - 1}}{\gamma}, \quad (16)$$

$$\phi_p = \arctan\left(\frac{\Im(k_z) + (\gamma - 2)/2H\gamma}{\Re(k_z)}\right), \quad (17)$$

$$\phi_v = \phi_p, \quad (18)$$

$$\phi_\rho = \arctan\left(\frac{\Im(k_z) - \frac{1}{2H} + \frac{(\gamma - 1)(c_s^2 k_\perp^2 / \omega^2)}{\gamma H}}{\Re(k_z)}\right). \quad (19)$$

Here, $A = 300 \text{ m s}^{-1}$ is the driver amplitude, which agrees with photospheric Doppler oscillations from the contribution of p -modes (R. L. McClure et al. 2019). This amplitude is also weaker than the rotational flow applied at the footpoint, which also increases with time (see Figure 2(a)). The amplitudes for the velocity, pressure, and density perturbations are denoted as $|v|$, $|P|$, and $|\rho|$, respectively; H is the pressure scale height; $\gamma = 5/3$ is the adiabatic index for a monatomic gas; k_\perp is the horizontal wavenumber of the driven waves; k_z is the vertical wavenumber, which only has a real part in our case; and $\omega = 2\pi/T$ is the driver frequency, with period $T = 370 \text{ s}$, which is within the typical range of p -mode periods. The variables ϕ_v , ϕ_p , and ϕ_ρ are the velocity, pressure, and density phase shifts compared to the vertical velocity perturbation, \hat{v}_z . The acoustic cutoff and thermally modified acoustic cutoff frequencies are denoted as ω_c and ω_g , respectively, where θ_B is the angle between the magnetic field and the direction of gravitational acceleration. The angle of the driver with respect to the vertical axis is represented by θ and is taken to be $\theta = 15^\circ$ in order to excite nonaxisymmetric modes (Y. Gao et al. 2023; S. J. Skirvin et al. 2023b).

The driver is applied locally at only one footpoint at the base of the domain and located inside the vortex tube. This is achieved by multiplying Equations (3)–(7) by the function

$$D(r) = \exp\left(-\frac{r^2}{\sigma^2}\right), \quad (20)$$

where σ is the standard deviation of the Gaussian profile describing the width of the driver, which in this study is taken to be $\sigma = 2 \text{ Mm}$. At the photospheric base of the domain, the full width at half-maximum (FWHM) of the Gaussian magnetic field strength is located at $r = 2.58 \text{ Mm}$; therefore, the driver can be considered to be applied within the footpoint of the vortex tube.

In order to investigate MHD wave propagation in the simulated vortex tube, we run two simulations, one with the photospheric wave driver and one without the wave driver.

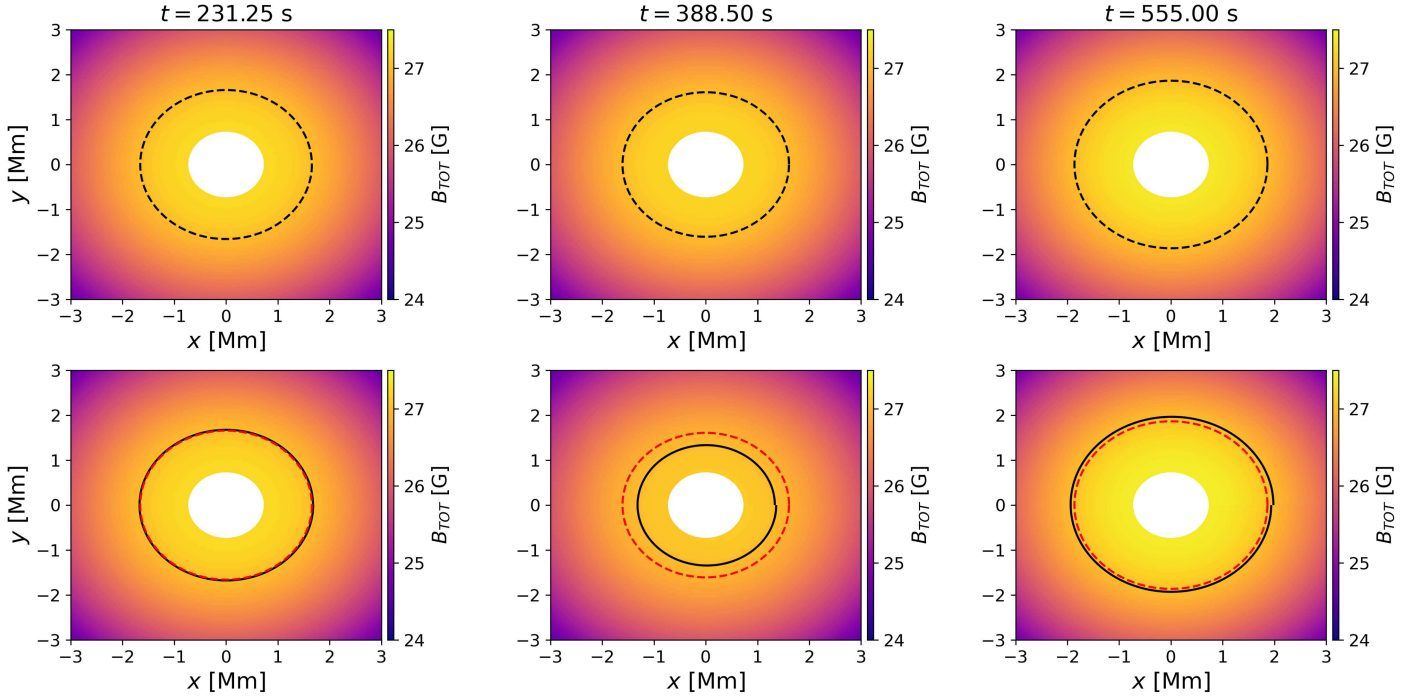


Figure 5. 2D contours of the magnetic field strength in the corona at a height of $z = -23.14$ Mm. Three different time snapshots are shown in different columns. The top row shows the time snapshots from the simulation including a rotational flow but with no wave driver, whereas the bottom row highlights the simulation with a rotational flow and a photospheric wave driver. The black contours indicate a constant magnetic field contour of 27 G. The red dashed contours in the bottom panels indicate the same magnetic contour for the simulation without a wave driver (i.e., the contours shown in the top panel).

Therefore, by subtracting the simulation without the wave driver from the simulation with the wave driver, we can study the effect of the driven perturbations within the vortex. It is important to note, however, that this is not equivalent to a linearization and that all nonlinear effects will still be included. Moreover, we run an additional simulation with the inclusion of the photospheric wave driver but without the additional rotational flow described in Section 2.3; this will allow us to compare the properties of MHD waves in the presence of a rotational plasma flow to a setup without such a background flow.

3. Results

3.1. Wave Decomposition

In full 3D simulations, where the magnetic field is not confined to a 2D geometry, the isolation of MHD waves becomes nontrivial as there are an infinite number of vectors normal to the magnetic field vector (N. Yadav et al. 2022). To help distinguish between the different types of waves in our simulation, we decompose motions relative to circular contours of constant magnetic field strength (J. M. Riedl et al. 2019; S. J. Skirvin & T. Van Doorselaere 2024). The conversion of components from a cylindrical geometry (r, φ, z) to those parallel, perpendicular, and azimuthal to magnetic flux surfaces is given by

$$\mathbf{e}_{\parallel} = \left[\frac{B_r \cos(\varphi)}{\sqrt{B_r^2 + B_z^2}}, \frac{B_r \sin(\varphi)}{\sqrt{B_r^2 + B_z^2}}, \frac{B_z(\varphi)}{\sqrt{B_r^2 + B_z^2}} \right], \quad (21)$$

$$\mathbf{e}_{\phi} = [-\sin(\varphi), \cos(\varphi), 0], \quad (22)$$

$$\mathbf{e}_{\perp} = \mathbf{e}_{\phi} \times \mathbf{e}_{\parallel}, \quad (23)$$

where \mathbf{e} denotes a unit vector in each direction, respectively. Equations (21)–(23) set up a Cartesian basis describing the vector decomposition with respect to magnetic field lines for an equilibrium magnetic field that is structured in the r - and z -directions in a cylindrical geometry. The component of the magnetic field azimuthal to magnetic surfaces is ignored in the decomposition due to the field lines being circularly symmetric around the axis of the vortex tube, and uniform rotational velocity is considered in the initial model (independent of φ). Moreover, the pitch angle of the magnetic field remains very small ($B_z \gg B_{\varphi}$; see Figure 3), especially in the plasma- $\beta \ll 1$ regime. This decomposition of components parallel, perpendicular, and azimuthal to the magnetic field lines will be important in the context of understanding the wave modes that are present in the simulation.

The validity of the decomposition described by Equations (21)–(23) in the presence of a background rotational flow or a weakly twisted magnetic field should be noted here. As the v_{φ} perturbation applied at the lower boundary is uniform in the azimuthal direction, and the wave driver amplitude is smaller than the background flow, it is suitable to assume that the contours of the constant magnetic field remain circular in a 2D cross-cut. This is also highlighted in Figure 5, where it is clear that, even in the presence of a background rotational flow, the constant magnetic field contours retain their circular outline throughout the duration of the simulation, such that Equations (21)–(23) remain valid for the present analysis. Therefore, any discussion regarding wave mode decomposition in this study will focus on the corona, where the magnetic field is untwisted ($B_z \gg B_{\varphi}$). Figure 5 highlights that the magnetic field naturally expands in the corona with time, even in the absence of a photospheric wave driver, due to the

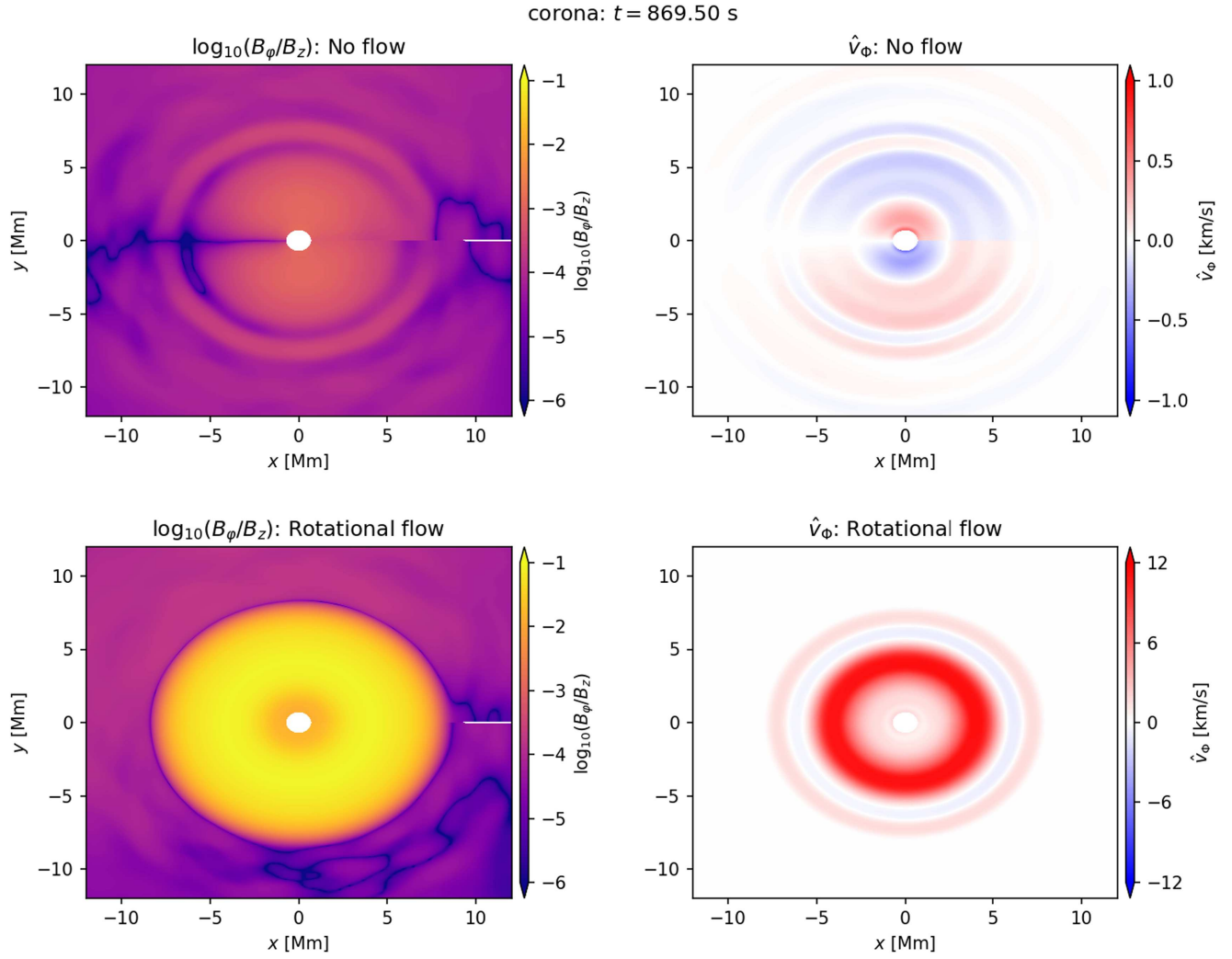


Figure 6. Horizontal cross-cuts at a coronal height ($z = -23.14$ Mm) displaying the logarithm of the ratio of the total azimuthal component of the magnetic field, B_ϕ , to the total vertical component of the magnetic field, B_z , as a proxy for the pitch angle of the magnetic field. In addition, we show the perturbed velocity tangential to constant magnetic contours \hat{v}_ϕ as defined in Equation (22). The top row shows the simulation with no rotational perturbation applied, whereas the bottom row indicates the case with a rotational flow at one footpoint. It should be noted that the color bar is saturated for the magnetic field (left-hand panels).

rotational flow creating a radial pressure gradient that causes the flux tube structure to slightly expand with time.

3.2. Velocity Perturbations

The magnetic contours in Figure 5 demonstrate the presence of the sausage mode within the vortex tube. This is evident in the bottom panels of Figure 5 through expanding and contracting of the contour of constant magnetic flux, reminiscent of a sausage mode in a cylindrical flux tube. The wave driver adopted in the current study is known to excite sausage modes (J. M. Riedl et al. 2021; S. J. Skirvin et al. 2023b). Moreover, vortex motions have been shown to excite sausage modes in flux tubes even in the absence of a wave driver (V. Fedun et al. 2011a). Therefore, this analysis provides further evidence of sausage modes supported by vortex tubes in the solar corona. Furthermore, the asymmetric wave driver also produces kink modes (J. M. Riedl et al. 2019; Y. Gao et al. 2023; S. J. Skirvin et al. 2023b); however, due to the vertical component of the perturbed velocity being considerably stronger than the horizontal components of the perturbed velocity, it is difficult to appreciate the horizontal displacement of the magnetic contours in Figure 5.

Using the decomposition method outlined in Section 3.1, we analyze the velocity perturbations tangential to circular contours of constant magnetic field strength. Figure 6 displays the total magnetic twist ($\log_{10}(B_\phi/B_z)$) and the \hat{v}_ϕ perturbation decomposition at a coronal height ($z = -23.14$ Mm) for the simulation without the rotational flow and the simulation with the rotational flow incorporated. It is important to note here that the B_ϕ component is still an order of magnitude weaker than the B_z component at this coronal height for the simulation with a rotational flow, further validating the decomposition outlined in Section 3.1. First, let us concentrate on the simulation without a rotational flow added. The nature of the wave driver described in Section 2.4 generates transverse (kink) waves inside the vortex tube (J. M. Riedl et al. 2019; Y. Gao et al. 2023; S. J. Skirvin et al. 2023b). When these motions are decomposed with respect to the magnetic flux surfaces outlined in Section 3.1, the clear asymmetric pattern of positive and negative fluctuations for $y > 0$ Mm and $y < 0$ Mm highlights the nature of the linearly polarized kink mode (top right panel of Figure 6). This is further understood when looking at Figure 3 in the study by M. Goossens et al. (2014) highlighting the rotational component of kink modes.

The B_ϕ in this case is purely a result of the kink mode perturbation and is much weaker than the ambient total magnetic field. However, for the simulation with the addition of a rotational plasma flow, the total magnetic twist is stronger and directed in one orientation. The driven waves in the rotational plasma flow, when decomposed tangential to flux surfaces, display a very different pattern to the scenario of a flux tube in the absence of rotational flow. The bottom right panel of Figure 6 shows the \hat{v}_ϕ decomposition of the motions in the simulation with a rotational flow and a wave driver. The resulting perturbations closely mimic those expected from torsional Alfvén waves, in the sense that they exhibit periodic twisting motions that are azimuthally symmetric (also see Figure 3 of M. Goossens et al. 2014). However, it is naive to interpret these motions as an indication of the presence of torsional Alfvén waves in the simulation as any torsional Alfvén waves generated by the nonstationary rotational flow would still produce one sign of the velocity perturbation (i.e., either positive or negative) instead of an oscillatory signal. However, it is evident that there is an oscillatory signal present, which suggests that these motions arise from the wave driver implemented at the bottom boundary. Instead, these perturbations more likely hint at the presence of sausage modes present within the vortex tube. As discussed earlier, the wave driver is known to produce sausage modes within the vortex tube (J. M. Riedl et al. 2021); however, it has been shown that sausage modes in twisted magnetic flux tubes can also produce azimuthal perturbations (I. Giagkiozis et al. 2015) with similar signatures to torsional Alfvén waves.

3.3. Azimuthal Wavenumbers

To investigate the MHD modes supported by the simulated vortex tube, we can apply a local Fourier decomposition to quantify the contribution of different azimuthal wavenumbers in our simulation. We employ a discrete Fourier transform to analyze the contribution of the different azimuthal wavenumbers using the profiles of \hat{v}_r and \hat{v}_ϕ as a function of angle at a fixed radial location (J. Terradas et al. 2018; N. Magyar et al. 2022; S. J. Skirvin et al. 2023b). The notation m is adopted to represent the excited azimuthal wavenumbers in the simulation and should not be confused with the eigenmode solutions. It is then possible to write the discrete Fourier transform, namely, the function g , on each flux surface as

$$G(m) = \frac{1}{N} \sum_{k=0}^{N-1} g(k) e^{-i \frac{2\pi}{N} mk} \quad (24)$$

for a discrete set of N samples ($m = 0, \dots, N-1$). In our case, the analysis is in the azimuthal direction, ranging from 0 to 2π . This means that instead of using k , it is more convenient to introduce the parameter $\theta_k = 2\pi k/N$. The contribution of each excited wave mode p to the total signal can be expressed, using the inverse Fourier transform, as

$$g(\theta_k) = \sum_{m=0}^{N-1} G(m) e^{im\theta_k}. \quad (25)$$

Unlike previous analyses (J. Terradas et al. 2018; N. Magyar et al. 2022; S. J. Skirvin et al. 2023b), the spectrum of excited azimuthal modes is no longer symmetric about $N/2$; hence, the Fourier transforms of the signals \hat{v}_r and \hat{v}_ϕ are no longer purely real or imaginary, corresponding to cosine and sine

components, respectively, for the simulation with a rotational flow applied. This result is easy to understand as the rotational flow breaks the azimuthal symmetry for the perturbed signals, which can no longer be separated into solely sine or cosine functions; instead, they are represented by a combination of even and odd functions that can be modeled by both sine and cosine functions.

The disparity of the resulting Fourier signals is highlighted in Figure 7, where the Fourier coefficients for \hat{v}_r and \hat{v}_ϕ are displayed for simulations both with and without a rotational flow. It is evident from Figures 7(a) and 7(b) that when no rotational flow is present, the azimuthal signals neatly decompose into even and odd functions for \hat{v}_r and \hat{v}_ϕ , respectively, highlighting the presence of sausage and kink modes resulting from the wave driver. However, when a rotational flow is present, there is significant power in both the real and imaginary Fourier coefficients as displayed in Figures 7(c) and 7(d). Furthermore, in the presence of a background rotational flow, significant power is associated with the axisymmetric $m = 0$ mode in the decomposed real \hat{v}_r and \hat{v}_ϕ signal. The Fourier analysis allows us to distinguish the MHD modes present by comparing the periodicities of these signals. For example, the $m = 0$ mode identified in the real \hat{v}_r signal is evidence of the sausage mode resulting from the photospheric wave driver and supported by the vortex tube. This is clear because the period of this signal is equivalent to the period of the higher-order modes (e.g., the $m = 1$ kink mode), which is only generated by the photospheric wave driver. On the other hand, the strong $m = 0$ coefficient in the real \hat{v}_ϕ signal is evidence of the torsional Alfvén wave resulting from the temporal behavior of the rotational flow applied at the photospheric footpoint in the simulation. This can be seen by comparing the periodicity of this signal with that displayed in Figure 2(a) and appreciating that these motions will possess a time lag when observed in the corona as displayed in Figure 7(d). We can calculate the crossing time required for an Alfvén wave to travel to this height given that the Alfvén speed below the TR is around $10\text{--}15 \text{ km s}^{-1}$ and the TR is positioned approximately 6 Mm above the bottom boundary. This results in a time lag of roughly 400–600 s, agreeing with the lag observed by comparing Figures 7(b) and 7(d). As the time derivative of the rotational flow is nonzero, it generates incompressible torsional oscillations that propagate within the vortex tube as torsional Alfvén waves (or pulses).

Further evidence of this mode being interpreted as a torsional Alfvén mode arising from the nonsteady flow applied at the lower boundary can be determined by examining the Fourier coefficients of the magnetic field perturbation. If a torsional Alfvén wave/pulse were excited, then we should also expect to see a similar signal in the axisymmetric mode from the magnetic field perturbation. Figure 8 displays the Fourier coefficients of the \hat{B}_r and \hat{B}_ϕ components for the simulations in the presence of a rotational flow both with and without an additional photospheric wave driver. Figure 8 shows the different periodicities that arise from the applied rotational flow and the implemented wave driver. The axisymmetric perturbations from the torsional Alfvén pulses generated from the nonsteady rotational flow are evident in the decomposition of the azimuthal magnetic field perturbation. The signals in both the \hat{v}_ϕ and \hat{B}_ϕ (real) coefficients for the axisymmetric mode appear at the same moment in time ($t = 500$ s) for the

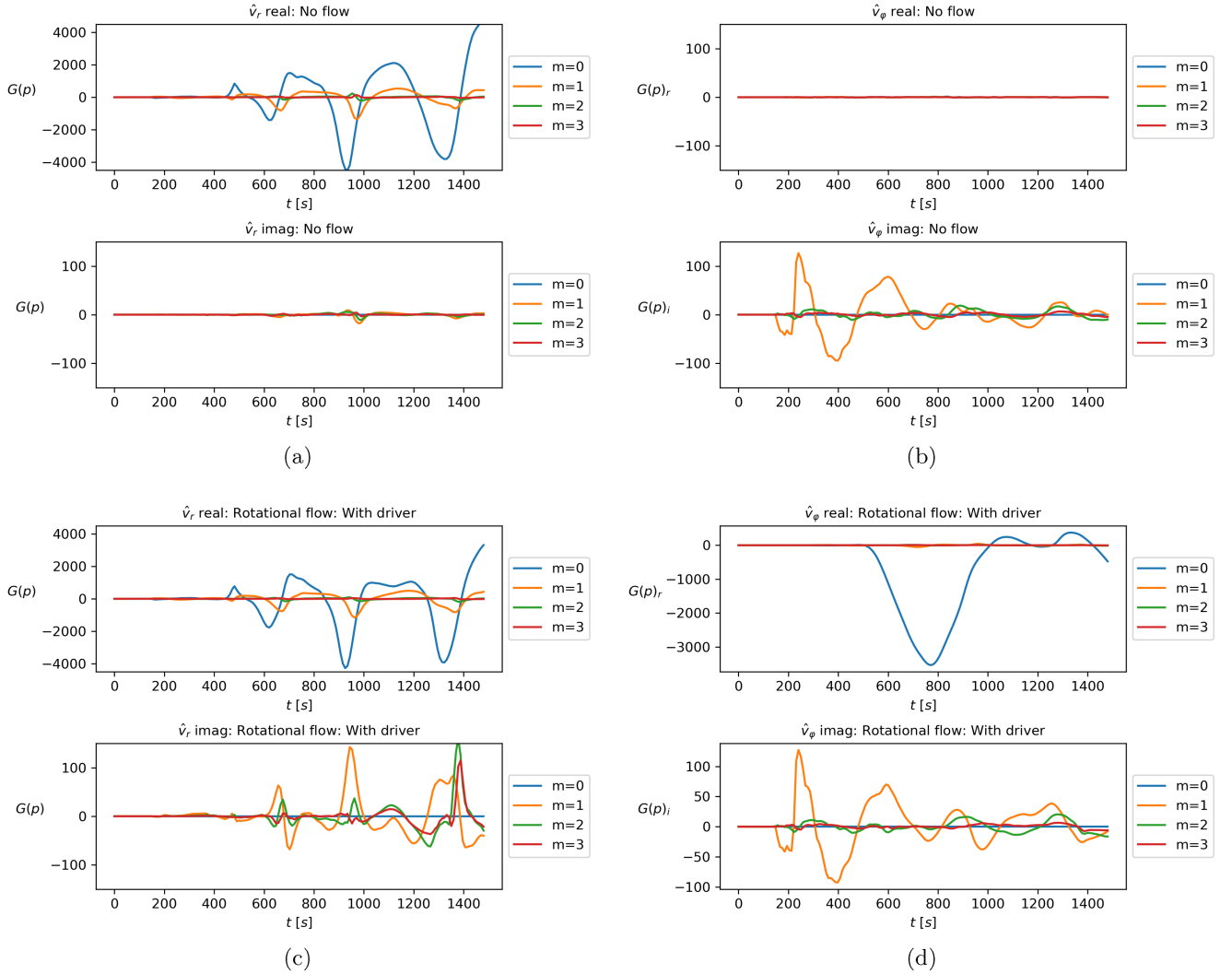


Figure 7. The real and imaginary Fourier coefficients of \hat{v}_r and \hat{v}_ϕ in the corona ($z = -23.14$ Mm) around flux surfaces at a radial location of $r = 7.20$ Mm. Panels (a) and (b) show the Fourier coefficients for the simulation without a rotational flow (i.e., just a photospheric wave driver), same as S. J. Skirvin et al. (2023b), for \hat{v}_r and \hat{v}_ϕ , respectively. Panels (c) and (d) show the same components but for the simulation with both a rotational flow and a photospheric wave driver. The different azimuthal wavenumbers excited are represented by different colors, highlighted in the legend.

simulation with a rotational flow and a wave driver, suggesting that they arise from the same formation mechanism.

3.4. Transport of Poynting Flux

$$\mathbf{S} = -\frac{1}{\mu_0}(\mathbf{v} \times \mathbf{B}) \times \mathbf{B}. \quad (26)$$

As the Poynting flux, expressed in Equation (26) with μ_0 , the magnetic permeability of free space, provides an indication of the magnetic energy transport, it would be extremely beneficial to understand the manner in which the Poynting flux is transported through the simulated vortex tube and, if possible, to provide some insight into the transport of the Poynting flux from MHD waves guided by the structure. Figure 9 provides a snapshot near the end of the simulation of streamlines of the total Poynting flux in the vortex tube. It is evident that there is a large amount of Poynting flux near the base of the vortex tube, which is understandable as this is the location of the rotational flow at the bottom boundary. Moreover, the streamlines of the Poynting flux follow a helical trajectory in the corona, whereas the streamlines are

more circular and horizontal below the TR. A significant amount of Poynting flux is still present in the corona ($\approx 10 \text{ kW m}^{-2}$); however, this figure displays the total Poynting flux in the simulation containing contributions from the background motions and the Poynting flux carried by perturbations. It should be emphasized that a large majority of the total Poynting flux in the simulation is a result of the background flow incorporated in the simulation (i.e., can be attributed to the rotating plasma itself).

Figure 10 displays vertical cuts of the z -component of the Poynting flux in the simulations with a photospheric driver both with and without a background rotational flow present. The left panel of Figure 10 shows the perturbed vertical component of the Poynting flux, \hat{S}_z , resulting from the waves driven by the driver applied locally at the lower boundary. It is evident that there is some leakage of magnetic energy below the TR in the chromosphere and that very little Poynting flux is channeled into the corona. This was a main conclusion by S. J. Skirvin & T. Van Doorselaere (2024; see also J. M. Riedl et al. 2021), who demonstrated that the majority of the energy flux is contained within the hydrodynamic component due to

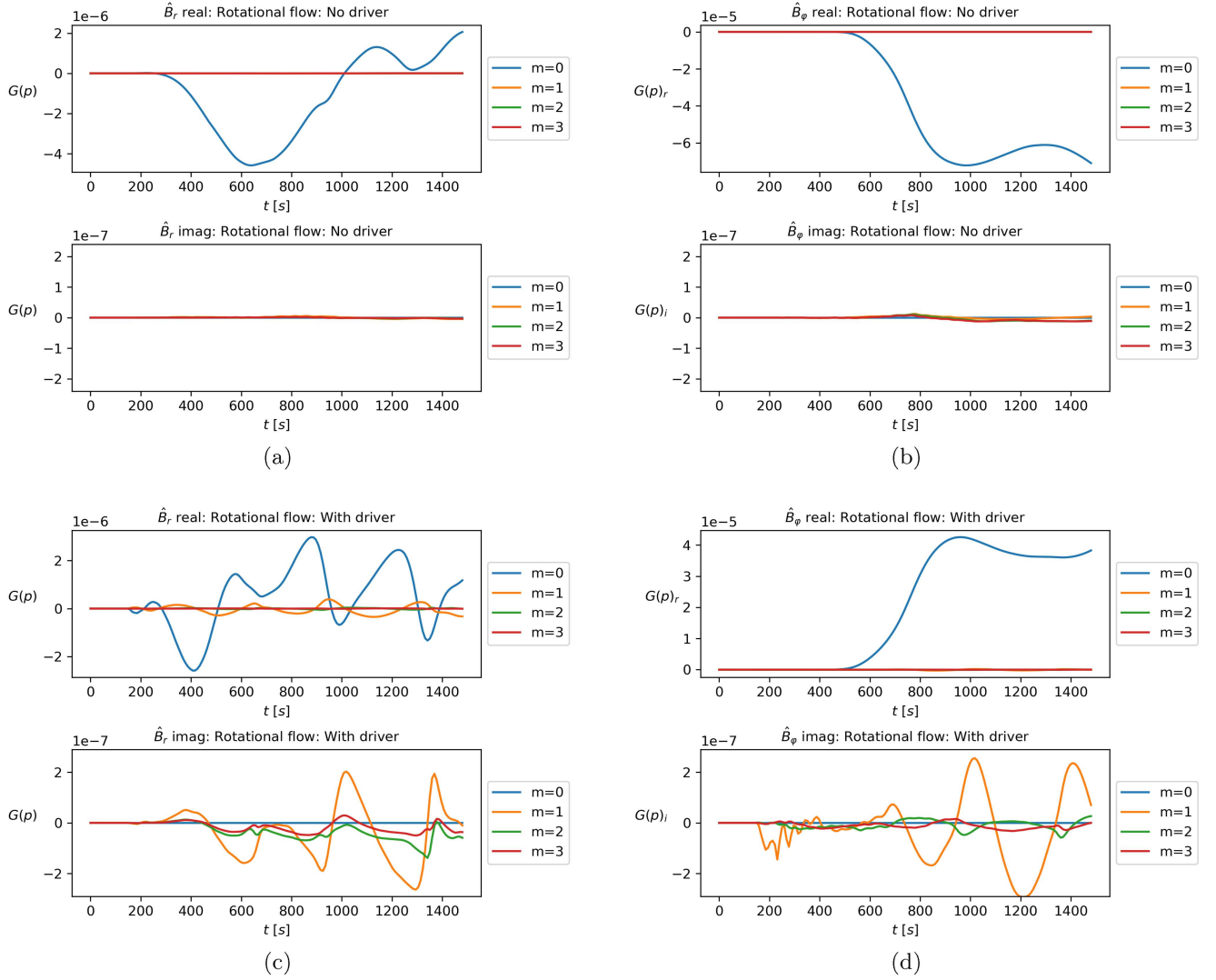


Figure 8. Real and imaginary Fourier coefficients of \hat{B}_r and \hat{B}_ϕ in the corona ($z = -23.14$ Mm) around flux surfaces at a radial location of $r = 7.20$ Mm. Panels (a) and (b) show the Fourier coefficients for the simulation of a rotational flow applied but with no photospheric wave driver. However, panels (c) and (d) display the magnetic field Fourier coefficients for the simulation with a rotational flow and an additional photospheric wave driver.

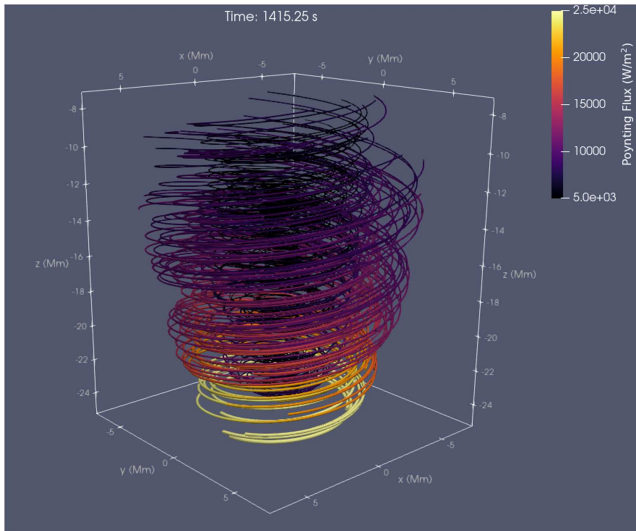


Figure 9. Snapshot at $t = 1415$ s of the 3D streamlines of the total Poynting flux in a box of the simulation domain. The magnitude of the Poynting flux is visualized through both the color and width of the 3D tube.

the nature of the driver and that wave energy is lost by lateral leakage in the chromosphere.

The middle panel of Figure 10 displays the total vertical component of the Poynting flux, S_z , in the simulation with a rotational flow and a wave driver. It is immediately apparent that there is a significantly greater amount of unsigned Poynting flux produced due to the rotational perturbation at the photosphere, and that this energy is channeled into the corona through the vortex tube. The right panel of Figure 10 displays the perturbed vertical component of the Poynting flux, \hat{S}_z , for the simulation with a rotational flow and a photospheric wave driver. A clear propagating signal is observed, and, strikingly, a remarkable increase in Poynting flux carried by perturbations is channeled into the corona. Not only is the magnitude of vertical Poynting flux associated with wave propagation greater in the presence of the vortex tube, the magnetic energy is channeled a greater distance into the coronal volume, highlighting the efficiency of solar vortex tubes to channel wave energy flux. This is attributed to the dynamical pressure resulting from the vortex flow, creating an overdense boundary layer that traps waves inside the vortex

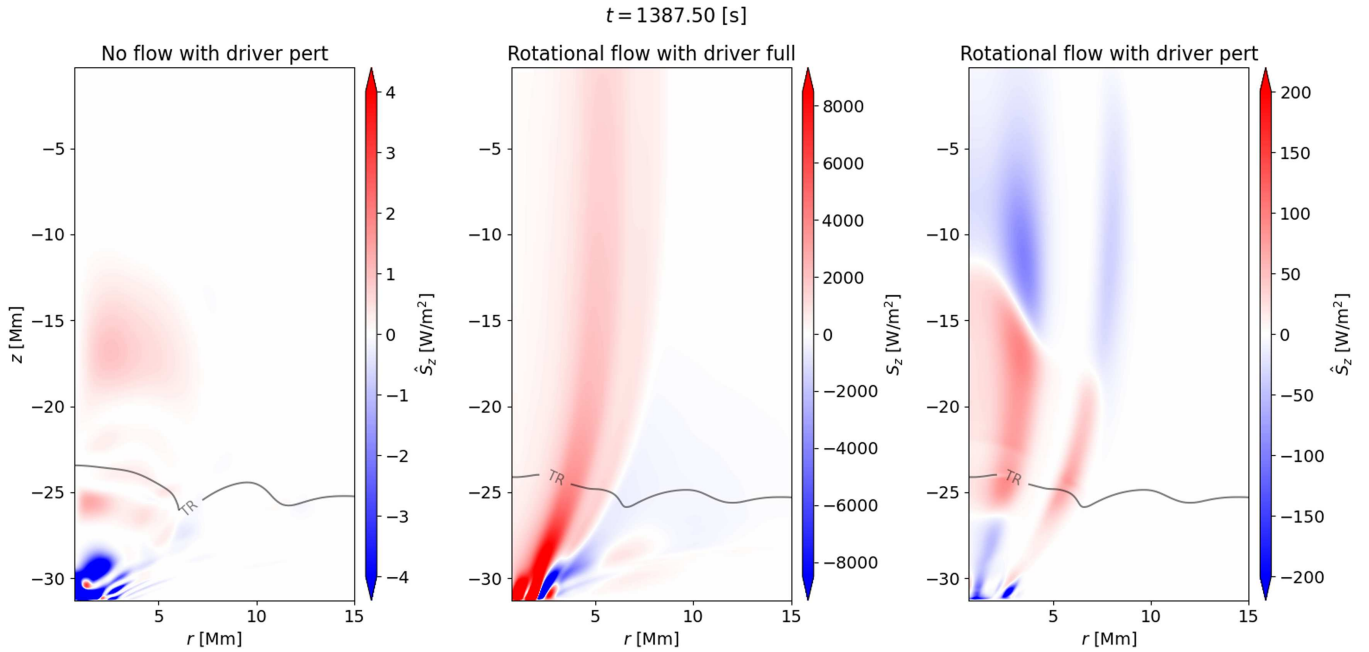


Figure 10. Vertical cuts for a snapshot at $t = 1388$ s at an angle of $\varphi = \pi/2$ for the perturbed (“pert” in subtitle) vertical component of Poynting flux \hat{S}_z in the simulation with no rotational flow (left panel). Middle panel: the total (“full” in subtitle) vertical component of the Poynting flux, S_z , for the simulation with a rotational flow and a wave driver. Right panel: the perturbed vertical component of the Poynting flux, \hat{S}_z , for the simulation with a rotational flow and a wave driver. The height of the TR is highlighted by the gray contour, and the color bar is saturated in all plots.

tube. For comparison, the maximum absolute value of S_z in the left panel of Figure 10 is 176 W m^{-2} , whereas the maximum absolute value of S_z in the right panel of Figure 10 is 386 W m^{-2} . Therefore, at the footpoint, the ratio between the maximum value of S_z in the two simulations (with and without the rotational flow) is roughly a factor of 2. However, it is clear that this ratio is different in the corona, where there is much greater S_z in the simulation with a rotational flow, highlighting the effectiveness of the vortex tube at transporting magnetic energy flux. We can estimate the transmission of S_z into the corona, relative to the photosphere, for each simulation when the wave driver is present. From Figure 10, we can conclude that the unsigned S_z in the corona when no rotational flow is included is of the order of 1 W m^{-2} . On the other hand, when a rotational flow is present, the unsigned S_z in the corona is roughly $50\text{--}100 \text{ W m}^{-2}$. This results in a transmission coefficient of 0.6% for the simulation with no rotational flow included and a transmission coefficient of 13%–26% when a rotational flow is present.

It could be assumed that the strong increase in perturbed vertical Poynting flux may be associated with the torsional Alfvén waves excited by the nonstationary rotational motion at the footpoint. However, Figure 11 does not suggest that the Poynting flux propagates at the Alfvén speed; instead, the vertical Poynting flux propagates at a speed closer to the local sound speed, suggesting that the \hat{S}_z is carried by slow magnetoacoustic waves. On the other hand, there is a coupling between slow magnetoacoustic and Alfvén waves relating to physical effects such as field line curvature, resonances, and shocks (J. V. Hollweg 1971; K. G. Ivanov & L. V. Evdokimova 1976; A. D. Crouch & P. S. Cally 2005), which may cause the Alfvén waves to have an indirect effect on the generated \hat{S}_z propagating with the local sound speed.

Recent work by S. J. Skirvin et al. (2024a) has shown that MHD waves carry increased amounts of \hat{S}_z when in the

presence of a background rotational flow. They demonstrate how the increase in Poynting flux associated with the waves depends on the amplitude ratio between the strength of the background flow and the strength of the perturbation. From Figure 2(a), we can assume that the amplitude ratio $v_0/\hat{v} = 5\text{--}10$, where v_0 denotes the background flow strength and \hat{v} denotes the strength of the perturbation. This amplitude ratio should correspond to an increase in \hat{S}_z of roughly 10%–20% for sausage modes and 20%–100% for kink modes. It is evident that the perturbed Poynting flux present in the right panel of Figure 10 is much greater than this predicted increase, suggesting the presence of other MHD modes in the simulation. On the other hand, the increase in S_z may also be due to the waves propagating in a different plasma environment when the rotational flow is included, as highlighted in Figure 4. It is possible that the Poynting flux associated with sausage and kink modes is increased in the simulation when compared to a scenario without a rotational flow present; however, accurately tracing the Poynting flux transported by these exact modes is extremely complex.

Figure 11 displays time–distance plots of the vertical component of the Poynting flux associated with the perturbations (waves), \hat{S}_z , in the simulations both with and without the inclusion of a background rotational plasma flow. In these plots, the trajectories of the local Alfvén and sound speeds are shown, and it is clear that in both simulations, the \hat{S}_z propagates at the local sound speed in a low- β plasma. The time–distance plots also demonstrate how the magnitude of \hat{S}_z increases when in the presence of a background rotational flow. Panel (b) in Figure 11 displays the full value for the vertical Poynting flux in the simulation with a rotational flow and a wave driver, and the same quantity is shown in panel (d), where values with absolute magnitudes greater than 100 W m^{-2} have been masked. In this plot, the initial background motions are evident as Poynting flux is present

$$r = 1.34 \text{ Mm}, \quad \varphi = 90.4^\circ$$

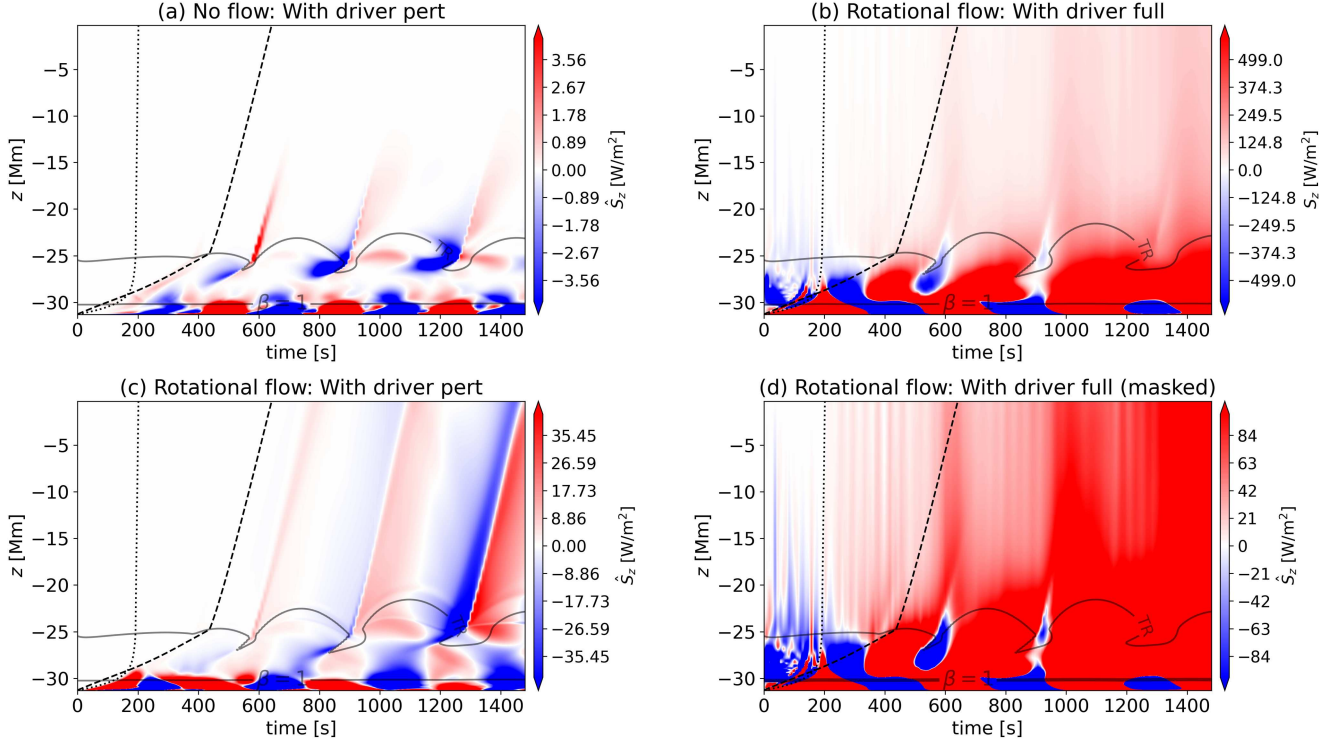


Figure 11. Time–distance plots at a radial location of $r = 1.34 \text{ Mm}$ and an azimuthal angle of $\varphi = 90.4^\circ$ of the vertical Poynting flux. Panel (a) shows the perturbed vertical Poynting flux, \hat{S}_z , in the simulation without a background rotational flow but with a wave driver (see, e.g., S. J. Skirvin et al. 2023b, 2024b). Panel (b) displays the full vertical Poynting flux S_z in the simulation with a background rotational flow and a wave driver. Panel (c) highlights the perturbed vertical Poynting flux in the simulation with a rotational flow and a wave driver (i.e., after the rotational flow simulation is subtracted). Panel (d) is the same as panel (b), but values with absolute magnitude greater than 100 W m^{-2} have been masked. The dotted line shows the trajectory of the local Alfvén speed, whereas the dashed line highlights the sound speed. The height of the TR and the plasma- $\beta = 1$ layer are denoted by the labeled contours, and the color bar is saturated in all plots.

before waves have entered the coronal volume; however, it is also clear that waves are generated by the rotational flow appearing at later times and propagate with the local Alfvén velocity. There is a high-frequency component present in the S_z signal that propagates at the Alfvén speed and appears to be an Alfvén wave/pulse whose origin is unclear. This signal is observed at smaller radii where the magnetic field at the footpoint is stronger and the transverse inhomogeneity is larger. As this high-frequency signal is not present in panel (c) after the rotational flow has been subtracted, it suggests that the high-frequency S_z signal traveling at the Alfvén speed is a nonlinear response of the interaction between the rotational flow and the stratified flux tube.

Panel (c) in Figure 11 shows the perturbed vertical component of the Poynting flux (i.e., after the rotational flow has been subtracted). Interestingly, \hat{S}_z shows extremely similar characteristics to propagating disturbances (PDs) associated with the TR dynamics (T. Samanta et al. 2015; S. J. Skirvin et al. 2024b). This has recently been discussed by S. J. Skirvin et al. (2024b), who demonstrated that the PDs are predominantly acoustic in nature, propagate along the magnetic field at the local sound speed, and, as a result, can be associated with slow magnetoacoustic waves. They have been shown to carry into the corona sufficient hydrodynamic energy flux ($>100 \text{ W m}^{-2}$) to contribute to the heating of local plasma; however, in the presence of a background plasma flow, the PDs also carry the same order of magnetic energy flux into the corona, which is injected directly at the TR. While slow magnetoacoustic waves carry zero net Poynting flux in the

linear regime, it is evident that the unsigned \hat{S}_z associated with these slow magnetoacoustic waves is larger when a background (rotational) plasma flow is present.

Panels (b) and (d) in Figure 11 highlight the positive vertical Poynting flux associated with the background rotational flow, and the waves, generated through the interaction of the loop with the flow itself, are transporting magnetic energy upward into the corona. The positive sign of the Poynting flux can be understood by looking at Equation (33) from S. J. Skirvin et al. (2024a) and repeated here:

$$[(\mathbf{v}_0 \times \mathbf{B}_0) \times \mathbf{B}_0]_z = \underbrace{(B_{0,\varphi} v_{0,z})}_{T1} - \underbrace{(v_{0,\varphi} B_{0,z})}_{T2} B_{0,\varphi}. \quad (27)$$

Equation (27) represents the vertical component of the Poynting flux associated with background motions only (i.e., zeroth order), subscripted with 0. There are two terms inside the bracket that, when combined with the sign of the background magnetic twist $B_{0,\varphi}$, determine whether the Poynting flux is directed upward or downward. The numerical values of these two terms in Equation (27) are displayed in Figure 12. It is evident that term 2 is greater than term 1 throughout the duration of the simulation; therefore, the overall sign of the terms inside the bracket is negative. However, the value of the background magnetic twist is negative, which results in a positive vertical Poynting flux associated with the rotational flow. If the rotational flow is introduced in the opposite direction, then $B_{0,\varphi}$ will be positive, but term 2 in Equation (27) will become negative, as $v_{0,\varphi}$ will change sign. Therefore, this scenario will still result in a

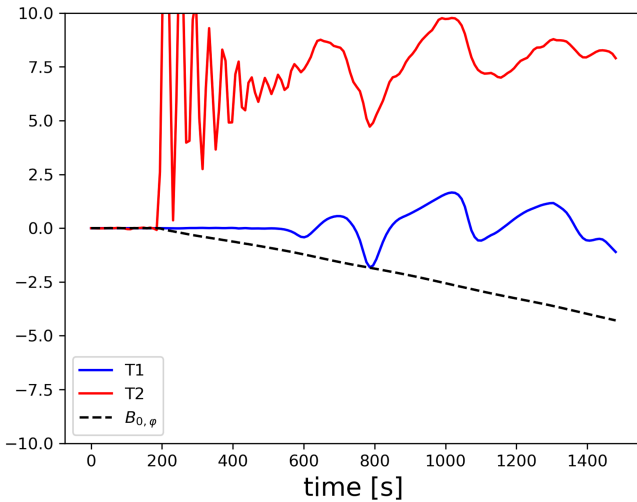


Figure 12. The numerical values of the two terms, T1 (blue) and T2 (red), inside the bracket of Equation (27) over time. Also shown is the background magnetic twist $B_{0,\varphi}$ in units of gauss. This figure is produced at a fixed position of $r = 1.34$ Mm, $\varphi = \pi/2$, and $z = -23.14$ Mm.

positive S_z , regardless of the direction of the rotational flow at the photosphere, because term 2 is always greater than term 1. This is only valid when term 1 plays a small role, in the case when $B_{0,\varphi} \ll B_{0,z}$, as is true for the current simulation. The implication in a strongly twisted tube is a different story, and it may no longer be possible to produce a net upward Poynting flux in strongly twisted tubes.

4. Discussion and Conclusions

In this study, we have performed a 3D numerical simulation aimed at generating a solar vortex tube and driving various MHD waves at the photosphere. A combination of sausage, kink, and torsional Alfvén waves is supported by the vortex tube as a result of both the photospheric wave driver and the nonstationary nature of the photospheric vortex flow. These waves are present in the simulation arising from different physical mechanisms—all of which are feasible in the solar atmosphere. The tube modes (e.g., kink and sausage) are produced by perturbations at the photosphere from p -modes that are absorbed by the magnetic flux tube, whereas the torsional Alfvén modes are generated by the rotational flow at the footpoint, which is nonstationary (i.e., has a nonzero time derivative).

We have demonstrated that it becomes difficult to accurately decompose different MHD modes when background rotational flows are present, and that some wave signatures may be misleading when compared to the classical understanding of waves in a uniform magnetic flux tube. For example, the sausage mode and torsional Alfvén mode display very similar characteristics when their motions are decomposed relative to circular contours of constant magnetic field strength (I. Giagkiozis et al. 2015). Furthermore, we have presented a Fourier analysis of the azimuthal wavenumbers to highlight the disparity between the different Fourier coefficients, unlike the case when no background rotational flow is present. The fast Fourier transform analysis underlined the various MHD modes present in the simulation; however, it provided a clearer insight into the contribution of sausage, kink, and torsional Alfvén modes to the various azimuthal signals of different velocity components. The numerical model presented in the current

study, along with the incorporated rotational flow, provides a highly nonuniform and structured plasma, where identifying pure wave modes (e.g., slow, fast, Alfvén) using velocity field perturbation information becomes increasingly complex as the modes become coupled in such systems.

We have examined the Poynting flux carried by waves present in both simulations (with and without a background rotational flow). Our results indicate that the Poynting flux transported by MHD waves is greatly increased when propagating within a vortex tube compared to the simulation where no rotational flow is considered. As discussed in Section 2.3, the presence of a vortex flow increases the dynamical pressure at the boundary of the vortex tube, which creates a layer of dense plasma that acts as an effective waveguide to trap and guide wave energy. Furthermore, in the presence of rotational flow, we have shown that the Poynting flux has a helical structure (as reported by S. S. A. Silva et al. 2024), highlighting the need for careful analysis when trying to interpret the Poynting flux present in observations where all three components of the velocity and magnetic field may not be retrievable. There is clear upward Poynting flux transported by the Alfvén waves generated from the rotational flow at the photosphere. The perturbed vertical Poynting flux associated with the wave driver travels at the local sound speed in the corona and shares a striking resemblance to PDs discussed by S. J. Skirvin et al. (2024b), which may be connected to the Poynting flux connected with jets and compressible waves in the solar wind (S. D. Bale et al. 2019). While the magnitude of the unsigned flux carried by slow magnetoacoustic waves is much larger when a background rotational flow is present, future work should investigate the net flux carried by these waves that would be available for heating in the upper atmosphere. Future work should investigate the energy transported by individual modes (e.g., sausage/kink). This analysis will be complex as the presence of a rotational flow will couple different azimuthal modes. Alternative diagnostics should be employed to study the modes, and their energies, present in complex plasma configurations (see, e.g., A. Raboonik et al. 2024a, 2024b).





In the future, it is essential to understand the Poynting vector associated with MHD waves in the presence of background plasma flows, especially in the corona, where direct measurement is extremely difficult and the solar wind is nonnegligible. This will allow for accurate diagnosis of the wave energy flux available in, for example, transverse kink waves, which is commonly computed using a 1D approximation (S. Tomczyk et al. 2007; S. W. McIntosh et al. 2011). More detailed numerical simulations of MHD waves supported by vortex tubes, which are ubiquitous, in a realistic solar atmosphere are required to correctly diagnose the energy flux transported along the magnetic field in a 3D geometry. Further analytical and numerical investigations are needed to understand the effect of background flows on the magnetic energy flux carried by different MHD modes. This is essential in the solar corona, where these waves are in the presence of the solar wind, which may affect the available energy carried by these waves.

Acknowledgments

We are grateful to the referee for the thoughtful suggestions, which have greatly improved the quality of this manuscript. S.J.S. and V.F. are grateful for the Science and Technology Facilities Council (STFC) grants ST/V000977/1 and ST/

Y001532/1. V.F., G.V., and I.B. thank The Royal Society, International Exchanges Scheme, collaboration with Instituto de Astrofísica de Canarias, Spain (IES/R2/212183), International Exchanges Scheme (NSTC) collaboration with National Central University, Taiwan (IEC/R3/233017), Institute for Astronomy, Astrophysics, Space Applications and Remote Sensing, National Observatory of Athens, Greece (IES/R1/221095), and Indian Institute of Astrophysics, India (IES/R1/211123) for the support provided. V.F. would like to thank the International Space Science Institute (ISSI) in Bern, Switzerland, for the hospitality provided to the members of the teams on “The Nature and Physics of Vortex Flows in Solar Plasmas” and “Tracking Plasma Flows in the Sun’s Photosphere and Chromosphere: A Review & Community Guide.” V.F. and G.V. are grateful to the Institute for Space-Earth Environmental Research (ISEE, International Joint Research Program, Nagoya University, Japan) for the support provided.

ORCID iDs

Samuel J. Skirvin  <https://orcid.org/0000-0002-3814-4232>
 Viktor Fedun  <https://orcid.org/0000-0002-0893-7346>
 Gary Verth  <https://orcid.org/0000-0002-9546-2368>
 Istvan Ballai  <https://orcid.org/0000-0002-3066-7653>

References

- Bale, S. D., Badman, S. T., Bonnell, J. W., et al. 2019, *Natur*, **576**, 237
 Bonet, J. A., Márquez, I., Sánchez Almeida, J., Cabello, I., & Domingo, V. 2008, *ApJL*, **687**, L131
 Crouch, A. D., & Cally, P. S. 2005, *SoPh*, **227**, 1
 Curdt, W., & Tian, H. 2011, *A&A*, **532**, L9
 Fedun, V., Shelyag, S., & Erdélyi, R. 2011a, *ApJ*, **727**, 17
 Fedun, V., Shelyag, S., Verth, G., Mathioudakis, M., & Erdélyi, R. 2011b, *AnGeo*, **29**, 1029
 Finley, A. J., Brun, A. S., Carlsson, M., et al. 2022, *A&A*, **665**, A118
 Gao, Y., Guo, M., Van Doorselaere, T., Tian, H., & Skirvin, S. J. 2023, *ApJ*, **955**, 73
 Giagkiozis, I., Fedun, V., Erdélyi, R., & Verth, G. 2015, *ApJ*, **810**, 53
 Giagkiozis, I., Fedun, V., Scullion, E., Jess, D. B., & Verth, G. 2018, *ApJ*, **869**, 169
 Goossens, M., Soler, R., Terradas, J., Van Doorselaere, T., & Verth, G. 2014, *ApJ*, **788**, 9
 Guarrasi, M., Reale, F., Orlando, S., Mignone, A., & Klimchuk, J. A. 2014, *A&A*, **564**, A48
 Hollweg, J. V. 1971, *JGR*, **76**, 5155
 Ivanov, K. G., & Evdokimova, L. V. 1976, *Ge&Ae*, **16**, 777
 Jess, D. B., Jafarzadeh, S., Keys, P. H., et al. 2023, *LRSP*, **20**, 1
 Jess, D. B., Morton, R. J., Verth, G., et al. 2015, *SSRv*, **190**, 103
 Karamelas, K., & Van Doorselaere, T. 2024, *A&A*, **681**, L6
 Khomenko, E., & Cally, P. S. 2012, *ApJ*, **746**, 68
 Klimchuk, J. A. 2006, *SoPh*, **234**, 41
 Kuniyoshi, H., Shoda, M., Iijima, H., & Yokoyama, T. 2023, *ApJ*, **949**, 8
 Magyar, N., Duckenfield, T., Van Doorselaere, T., & Nakariakov, V. M. 2022, *A&A*, **659**, A73
 Magyar, N., Utz, D., Erdélyi, R., & Nakariakov, V. M. 2021, *ApJ*, **911**, 75
 McClure, R. L., Rast, M. P., & Martínez Pillet, V. 2019, *SoPh*, **294**, 18
 McIntosh, S. W., de Pontieu, B., Carlsson, M., et al. 2011, *Natur*, **475**, 477
 Mignone, A., Bodo, G., Massaglia, S., et al. 2007, *ApJS*, **170**, 228
 Mignone, A., Bodo, G., Vaidya, B., & Mattia, G. 2018, *ApJ*, **859**, 13
 Mignone, A., Zanni, C., Tzeferacos, P., et al. 2012, *ApJS*, **198**, 7
 Mihalas, D., & Mihalas, B. W. 1984, *Foundations of radiation hydrodynamics* (New York: Oxford Univ. Press)
 Morton, R. J., Verth, G., Fedun, V., Shelyag, S., & Erdélyi, R. 2013, *ApJ*, **768**, 17
 Murabito, M., Shetye, J., Stangalini, M., et al. 2020, *A&A*, **639**, A59
 Pelouze, G., Van Doorselaere, T., Karamelas, K., Riedl, J. M., & Duckenfield, T. 2023, *A&A*, **672**, A105
 Raboonik, A., Pontin, D. I., & Tarr, L. A. 2024a, *ApJ*, **977**, 191
 Raboonik, A., Tarr, L. A., & Pontin, D. I. 2024b, *ApJ*, **967**, 80
 Reale, F., Orlando, S., Guarrasi, M., et al. 2016, *ApJ*, **830**, 21
 Riedl, J. M., Van Doorselaere, T., Reale, F., et al. 2021, *ApJ*, **922**, 225
 Riedl, J. M., Van Doorselaere, T., & Santamaria, I. C. 2019, *A&A*, **625**, A144
 Samanta, T., Pant, V., & Banerjee, D. 2015, *ApJL*, **815**, L16
 Santamaria, I. C., Khomenko, E., & Collados, M. 2015, *A&A*, **577**, A70
 Serio, S., Peres, G., Vaiana, G. S., Golub, L., & Rosner, R. 1981, *ApJ*, **243**, 288
 Sharma, R., Verth, G., & Erdélyi, R. 2018, *ApJ*, **853**, 61
 Shelyag, S., Keys, P., Mathioudakis, M., & Keenan, F. P. 2011, *A&A*, **526**, A5
 Silva, S. S. A., Fedun, V., Verth, G., Rempel, E. L., & Shelyag, S. 2020, *ApJ*, **898**, 137
 Silva, S. S. A., Verth, G., Rempel, E. L., et al. 2024, *ApJ*, **963**, 10
 Skirvin, S., Verth, G., González-Avilés, J. J., et al. 2023, *AdSpR*, **71**, 1866
 Skirvin, S. J., Fedun, V., Goossens, M., Silva, S. S. A., & Verth, G. 2024a, *ApJ*, **975**, 176
 Skirvin, S. J., Fedun, V., Silva, S. S. A., et al. 2023a, *MNRAS*, **518**, 6355
 Skirvin, S. J., Gao, Y., & Van Doorselaere, T. 2023b, *ApJ*, **949**, 38
 Skirvin, S. J., Samanta, T., & Van Doorselaere, T. 2024b, *A&A*, **689**, A135
 Skirvin, S. J., & Van Doorselaere, T. 2024, *A&A*, **683**, A61
 Su, Y., Gömöry, P., Veronig, A., et al. 2014, *ApJL*, **785**, L2
 Terradas, J., Magyar, N., & Van Doorselaere, T. 2018, *ApJ*, **853**, 35
 Tomczyk, S., McIntosh, S. W., Keil, S. L., et al. 2007, *Sci*, **317**, 1192
 Tziotziou, K., Scullion, E., Shelyag, S., et al. 2023, *SSRv*, **219**, 1
 Tziotziou, K., Tsiropoula, G., & Kontogiannis, I. 2020, *A&A*, **643**, A166
 Tziotziou, K., Tsiropoula, G., Kontogiannis, I., Scullion, E., & Doyle, J. G. 2018, *A&A*, **618**, A51
 Van Doorselaere, T., Srivastava, A. K., Antolin, P., et al. 2020, *SSRv*, **216**, 140
 Wedemeyer, S., & Steiner, O. 2014, *PASJ*, **66**, S10
 Wedemeyer-Böhm, S., Scullion, E., Steiner, O., et al. 2012, *Natur*, **486**, 505
 Yadav, N., Cameron, R. H., & Solanki, S. K. 2020, *ApJL*, **894**, L17
 Yadav, N., Cameron, R. H., & Solanki, S. K. 2021, *A&A*, **645**, A3
 Yadav, N., Keppens, R., & Popescu Brăileanu, B. 2022, *A&A*, **660**, A21